Nanoscale

PAPER

View Article Online
View Journal

Cite this: DOI: 10.1039/d5nr00699f

Suspension stability of aluminum-based adjuvants†

Zhihui Liang,‡[a,b,c,f] Hongyang Gao,‡[a,b,c] Qian Ren,[d,e] Xin Li,[a,b,c] Yubin Ma,[a,b,c] Changying Xue*[d,e] and Bingbing Sun *[a,b,c]

Aluminum hydroxyphosphate (AAHP) and aluminum oxyhydroxide (AlOOH) are widely used adjuvants in human vaccines. However, vaccines formulated with aluminum-based adjuvants often exist as suspensions that can experience phase separation, spontaneous aggregation, layering, and settling, potentially compromising their immunogenic efficacy. Despite their widespread use, research into the suspension stability of aluminum-based adjuvants remains limited. In this study, we synthesized a series of aluminum hydroxyphosphate and AlOOH nanoparticles and systematically evaluated their suspension stabilities under various conditions. Our findings reveal that for aluminum hydroxyphosphate, particle size and ζ potential are the primary determinants of suspension stability, aligning with DLVO theory and Stokes' law. For AlOOH, the suspension stability is governed by a combination of factors, including particle size, ζ potential, surface free energy (SFE) and hydrophobicity. Notably, the commercial adjuvant Alhydrogel® exhibited low suspension stability compared to our synthesized AlOOH nanoparticles, a result attributed to its high SFE. Furthermore, under specific formulation conditions, aluminum-based adjuvants with enhanced suspension stability improved the suspension stability of their corresponding adjuvant-antigen complexes. This study provides a foundation for optimizing the suspension stability of aluminum-based adjuvants and offers valuable insights for their rational design and transportation in vaccine development.

Received 17th February 2025,
Accepted 2nd May 2025

DOI: 10.1039/d5nr00699f

rsc.li/nanoscale

1. Introduction

Adjuvants are generally formulated in subunit and certain inactivated vaccines to achieve more robust and durable immune responses.[1,2] Since the discovery of the adjuvanticity of aluminum salts in 1926, they have been extensively studied and widely formulated in authorized human vaccines in the past few decades.[2,3] Among them, aluminum hydroxyphosphate (AAHP) and aluminum oxyhydroxide (AlOOH) are the most frequently used aluminum-based adjuvants in human vaccines. AAHP is a chemically amorphous hydroxyphosphate aluminum salt with no fixed ratio of –OH and $-PO_4$,[4–6] while AlOOH is a crystalline salt.[7,8] Both adjuvants have been utilized in vaccines such as for DTaP, polio, Hib, Hepatitis B.[9]

Aluminum-adjuvanted vaccines are typically formulated as aqueous suspensions, however, they tend to undergo phase separation.[8,10–13] Furthermore, these vaccine products are often subjected to interfacial stresses during production, transportation, and administration. Such stresses can significantly alter the suspension profile, impacting vaccine stability and leading to adverse effects, including reduced antigen adsorption, difficulties in redispersion, and decreased immune efficacy.[10,14–16] In addition, failure to resuspend vaccines containing aluminum-based adjuvants after storage and transportation has been reported to diminish product availability.[10] Consequently, numerous studies have focused on enhancing the stability of vaccine suspensions. For example, it was reported that the introduction of stabilizing agents or surfactants can significantly improve the suspension stability of aluminum-based adjuvant-formulated vaccines. Moreover, the properties of nanoscale materials, *e.g.*, shape, surface charge and particle sizes, have been found to influence their suspension stability.[17,18] Bi *et al.*[19] demonstrated that nanoparticles with low surface free energy (SFE) exhibited excellent

[a]State Key Laboratory of Fine Chemicals, Dalian University of Technology, 2 Linggong Road, 116024 Dalian, China. E-mail: bingbingsun@dlut.edu.cn
[b]School of Chemical Engineering, Dalian University of Technology, 2 Linggong Road, 116024 Dalian, China
[c]Frontiers Science Center for Smart Materials Oriented Chemical Engineering, School of Chemical Engineering, Dalian University of Technology, 2 Linggong Road, 116024 Dalian, China
[d]MOE Key Laboratory Bio-Intelligent Manufacturing, Dalian University of Technology, 2 Linggong Road, 116024 Dalian, China. E-mail: changyingxue@dlut.edu.cn
[e]School of Bioengineering, Dalian University of Technology, 2 Linggong Road, 116024 Dalian, China
[f]Department of Biomedical Engineering, The Chinese University of Hong Kong, Shatin, New Territories, Hong Kong SAR

†Electronic supplementary information (ESI) available. See DOI: https://doi.org/10.1039/d5nr00699f

‡These authors made equal contributions to this work.

suspension stability. However, for aluminum-based adjuvants, how these factors affect their suspension stability remains unclear, which limits the adjuvant design and optimization of vaccine formulations.

In this study, two libraries of aluminum-based adjuvants were synthesized, *i.e.*, AAHP and AlOOH nanoparticles with controlled surface charges and aspect ratios, respectively. The results demonstrated that for AAHP nanoparticles (AAHP NPs), the suspension stability was dominated by particle sizes and ζ potential. The surface charges of AAHP NPs prevent the aggregation and enhance the suspension stability. For AlOOH nanorods, in addition to particle sizes and ζ potential, a lower SFE contributes to a stable suspension profile. Furthermore, the suspension stability of the adjuvant-antigen complexes aligns with that of the adjuvants, attributed to the shielding effect on the particle surface charges and the complexity of the adjuvant-antigen conjugates. This study highlights the key factors that contribute to the suspension stability of aluminum-based adjuvants and provides new insights in the design of vaccine adjuvants from a stability perspective.

2. Materials and methods

2.1 Materials

Adju-Phos® and Alhydrogel® were purchased from InvivoGen (San Diego, CA). Aluminum chloride hexahydrate ($AlCl_3{\cdot}6H_2O$) was purchased from Fisher Scientific (Loughborough, UK). Ethylenediamine (EDA) was purchased from Shandong Xiya Chemical Industry Co., Ltd (Shandong, China). Sodium phosphate tribasic (Na_3PO_4) was purchased from Shanghai Titan Scientific Co., Ltd (Shanghai, China). Aluminum(III) nitrate nonahydrate($Al(NO_3)_3{\cdot}9H_2O$) and sodium hydroxide (NaOH) were purchased from Sangon Biotech Co., Ltd (Shanghai, China). Human papillomavirus (HPV) VLP type 18 was purchased from Zerun Biotechnology Co., Ltd (Shanghai, China). Pyrene was purchased from RHAWN (Shanghai, China). Bovine Serum Albumin (BSA) was purchased from Sigma (MO, USA). All chemicals were of analytical grade and were used without further purification.

2.2 Synthesis of AAHP NPs

The synthesis method for AAHP NPs was based on our previous study.[6] Briefly, 3.237 g of $AlCl_3{\cdot}6H_2O$ and 3.977 g of Na_3PO_4 were each dissolved in 50 mL of deionized water. Under stirring at 590 rpm, the Na_3PO_4 solution was added dropwise into the $AlCl_3{\cdot}6H_2O$ solution until the desired pH was achieved. Stirring continued for additional 30 min, after which the resultant mixture was autoclaved at 121 °C for 30 min. The precipitate was then washed three times with deionized water.

2.3 Synthesis of AlOOH nanorods

The synthesis method for AlOOH nanorods was based on our previous study.[7] Briefly, 1.3933 g of $Al(NO_3)_3{\cdot}9H_2O$ was dissolved in 20 mL of deionized water. EDA was then added slowly under stirring at 400 rpm to adjust the pH to values between 4 and 6. The pH was monitored in real-time, and once the desired value was reached, stirring continued for additional 15 min. The reaction mixture was subsequently transferred into a 23 mL Teflon-lined stainless-steel autoclaves and subjected to hydrothermal treatment at 160 °C for 16 h. Following the hydrothermal process, the product was washed three times with deionized water.

2.4 Material characterization

The AAHP NPs and AlOOH nanorods were dispersed on carbon-coated copper grids and characterized using transmission electron microscopy (TEM, JEOL JEM-1200EX) at an acceleration voltage of 120 kV. The crystal structures of the nanoparticles were analyzed using a Philips X′pert X-ray diffraction (XRD, Rigaku D/Max 2400 type X-ray spectrometer) equipped with Cu Kα radiation (λ = 1.54178 Å). Diffractograms were recorded over a 2θ range from 10° to 80°. The hydrodynamic sizes and ζ potentials of the nanoparticles were measured by dynamic light scattering (DLS, Brookhaven, 90 plus PALS) after dispersion in water or saline.

2.5 Determination of suspension stability of AAHP NPs and AlOOH nanorods

The suspension stability of AAHP NPs was measured by UV-visible spectrophotometry.[19] Briefly, AAHP NPs were prepared at a concentration of 1.1 mg mL^{-1} in deionized water or normal saline, and then 2 mL of suspension was placed in a 10 mm quartz cuvette and monitored at 228 nm for 12 h. The measurement method for AlOOH nanorods was the same as that for AAHP NPs, with a measurement wavelength of 332 nm.

2.6 Determination of SFE of AlOOH nanorods

The SFE of nanoparticles was determined using the maximum particle dispersion (MPD) method.[20] Briefly, a series of ethanol–water solutions were prepared, with the ratio of ethanol to water ranging from 0 : 10 to 10 : 0. Then, nanoparticles were dispersed in the prepared ethanol–water solutions at a concentration of 2 mg mL^{-1}. After thorough mixing, the suspension was centrifuged, and the supernatant was collected for absorbance measurement at 400 nm. The SFE was determined based on the surface tension of the suspension with the maximum dispersion of nanoparticles.

2.7 Determination of hydrophobicity of AlOOH nanorods

The hydrophobicity of AlOOH nanorods was measured by the pyrene assay.[21–24] The AlOOH nanorods was re-suspended in H_2O and saline at different concentrations ranging from 0.2–1.1 mg mL^{-1}. The pyrene was dissolved in methanol and then eventually mixed with AlOOH nanorods to prepare a 2 μmol mL^{-1} solution. After shaking at 1000 rpm for 2 h in a metal bath at room temperature, the samples were analyzed using a fluorescence spectrophotometer (FS5, Edinburgh Instrument, UK). Excitation was performed at 332 nm, with emission detected across a range of 350–500 nm, employing

slit widths of 1.6 nm for both excitation and emission. The peak intensities at 371 nm (I_1) and 381 nm (I_3) were recorded and the I_1/I_3 ratio was calculated. In pyrene measurements, a lower I_1/I_3 ratio indicates that the NP is more hydrophobic.

2.8 Statistical analysis

All experiments were conducted in triplicate, and the values were presented as mean ± SD. Two-tailed student's *t*-test was used to determine statistical significance between the two datasets.

3. Results and discussion

3.1 Synthesis and characterization of AAHP NPs

AAHP NPs were prepared by using a chemical precipitation method through adjusting the molar ratio of $AlCl_3{\cdot}6H_2O$ (Al) to Na_3PO_4 (P).[6] The synthesized AAHP NPs exhibited a network of plate-like structures as observed through TEM (Fig. 1a). The morphology of the particles did not vary with the different ratio of phosphorus to aluminum. X-ray diffraction (XRD) analysis indicated that the synthesized AAHP NPs were amorphous (Fig. 1b), exhibiting a similarity to the commercially available adjuvant, Adju-Phos®. Further, the ζ potentials of the NPs were measured in water, showing a transition in surface charge from positive to negative with the increase of molar ratio of PO_4/Al. The as-prepared AAHP NPs exhibited surface charges of +20 ± 1 mV, −6 ± 1 mV, and −29 ± 2 mV (Table 1), and they were noted as AAHP-Posi, AAHP-Neut, and AAHP-Nega, respectively. The hydrodynamic sizes of the AAHP NPs ranged from 200 to 1200 nm in water (Table 1). AAHP-Neut exhibited the largest hydrodynamic size, while AAHP-Posi and AAHP-Nega showed much smaller hydrodynamic sizes. The possible reason is that a higher surface charge leads to stronger electrostatic interactions, which helps to prevent particle aggregations and consequently yield smaller hydrodynamic sizes.[25,26] As a control, Adju-Phos® exhibited a hydrodynamic size of 193 ± 9 nm and a surface charge of −19 ± 2 mV in water (Table 1).

Table 1 Hydrodynamic size and ζ potential of AAHP NPs in water measured by dynamic light scattering (DLS)

Sample ID	Hydrodynamic sizes in Water (nm)	Polydispersity index	Zeta potential in water (mV)
AAHP-Posi	219 ± 2	0.18 ± 0.03	+20 ± 1
AAHP-Neut	1193 ± 49	0.21 ± 0.02	−6 ± 1
AAHP-Nega	226 ± 8	0.22 ± 0.03	−29 ± 2
Adju-Phos®	193 ± 9	0.13 ± 0.06	−19 ± 2

3.2 Assessment of suspension stability of AAHP NPs and AAHP NPs-antigen complexes

The suspension stability of AAHP NPs with controlled surface charges was investigated by measuring their suspension stability indexes in water.[19,27,28] Overall, most samples exhibited good suspension stability in water, compared to that in saline buffer. The suspension stability indexes for AAHP-Posi, AAHP-Nega, and Adju-Phos® remained above 93% over a 12 hour period in water (Fig. 2a), indicating excellent suspension stability. Conversely, AAHP-Neut exhibited poor suspension stability, with its suspension stability index declining to 8% after 12 h (Fig. 2a). The stability of the samples was further monitored in saline buffer. The suspension stability index of AAHP-Posi decreased to 48% after 12 h, while AAHP-Neut, AAHP-Nega, and Adju-Phos® exhibited a rapid decline to ~10% within the first hour (Fig. 2b). This result was corroborated by the static snapshots of the samples in saline (Fig. S1, ESI†). After 6 h of static settling, AAHP-Posi remained in a relatively stable state without significant solid precipitation. In contrast, the other three formulations displayed significant solid precipitation within 0.5 h of settling, resulting in a clear supernatant after 6 h.

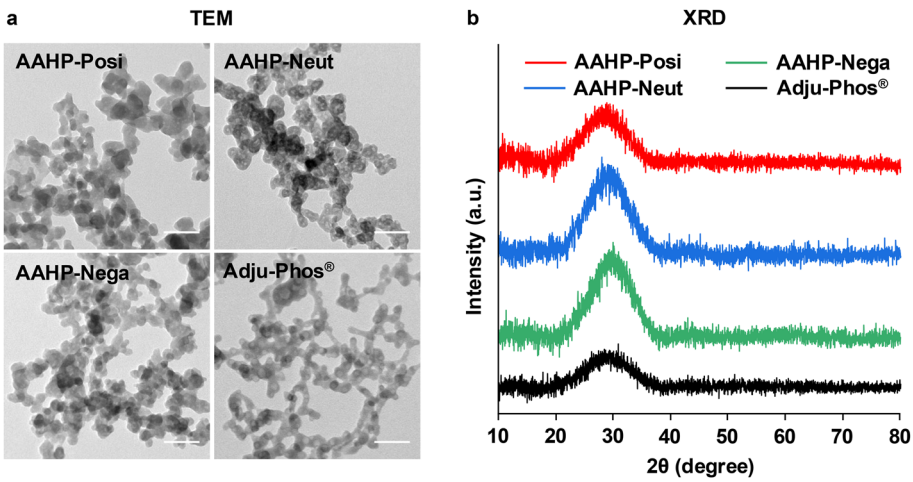

Fig. 1 Characterization of AAHP NPs. (a) TEM analysis of AAHP NPs. The scale bar is 100 nm. (b) XRD analysis of AAHP NPs. Adju-Phos® is used as a control.

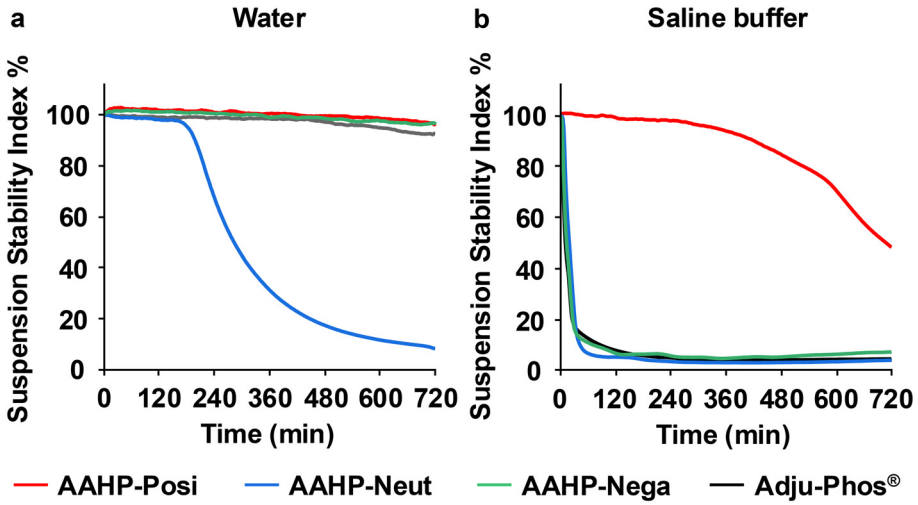

Fig. 2 Determination of the suspension stability of AAHP NPs. Suspension stability index of AAHP NPs in (a) water and (b) saline buffer.

Previous studies have established a correlation between practical formulation parameters, such as pH and ionic strength, and the sedimentation behavior of aluminum phosphate nanoparticles, with a reduction in surface charge identified as a key driver for aggregation.[10,11] In saline buffer, the hydrodynamic sizes and polydispersity index (PDI) of the nanoparticles increased, while the absolute value of ζ potentials decreased, approaching neutral (Fig. 3). This can be attributed to the elevated ionic strength in saline buffer, which shields the surface charges of the particles, thereby promoting particle attraction and aggregation.[29] Notably, the change in ζ potential was less pronounced for AAHP-Posi compared to AAHP-Nega. This may arise from the stronger charge neutralization and shielding effect exerted by of Na^+ on negatively-charged NPs, relative to the effect of Cl^- on positively-charged NPs. The smaller ionic radius of Na^+ compared to Cl^- likely enhances its ability to neutralize surface charges, resulting in a more significant ζ potential change for AAHP-Nega.[30] As the ζ potential approaches 0 mV, the reduction in surface charge diminishes electrostatic repulsion between particles, potentially shifting the dominant interparticle interactions from electrostatic to van der Waals attraction or hydrophobic interactions.[11] According to the DLVO theory,[31–33] a higher ζ potential enhances colloidal stability,[18,31,34] whereas a reduction in surface charge destabilizes the system, leading to particle aggregation and sedimentation. Furthermore, Stokes' law[17,18] underscores the importance of particle size in suspension stability, as smaller particles exhibit greater resistance to sedimentation due to the gravitational effects,[17,18,35,36] while larger particles are more prone to rapid sedimentation. Collectively, these findings demonstrate that particle size and surface charge are the primary determinants of the suspension stability of AAHP NPs.

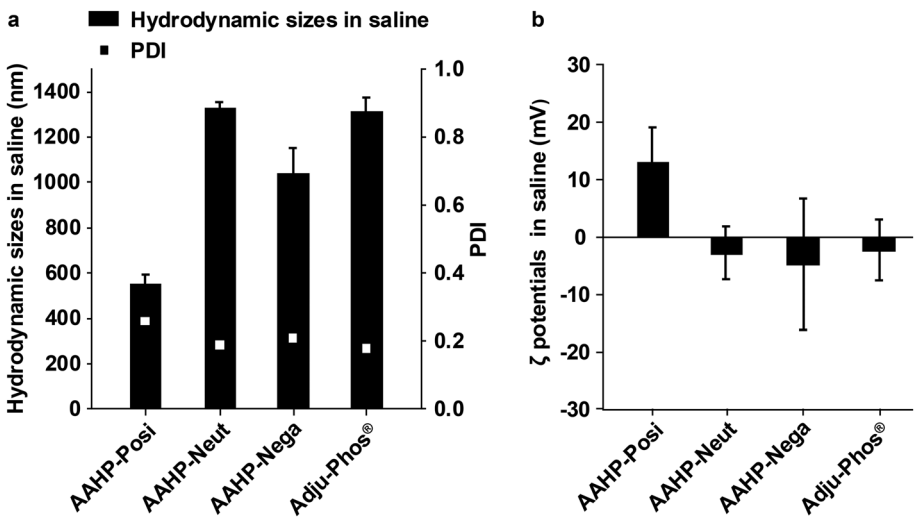

Fig. 3 (a) Hydrodynamic sizes, PDI, and (b) ζ potentials of AAHP NPs in saline.

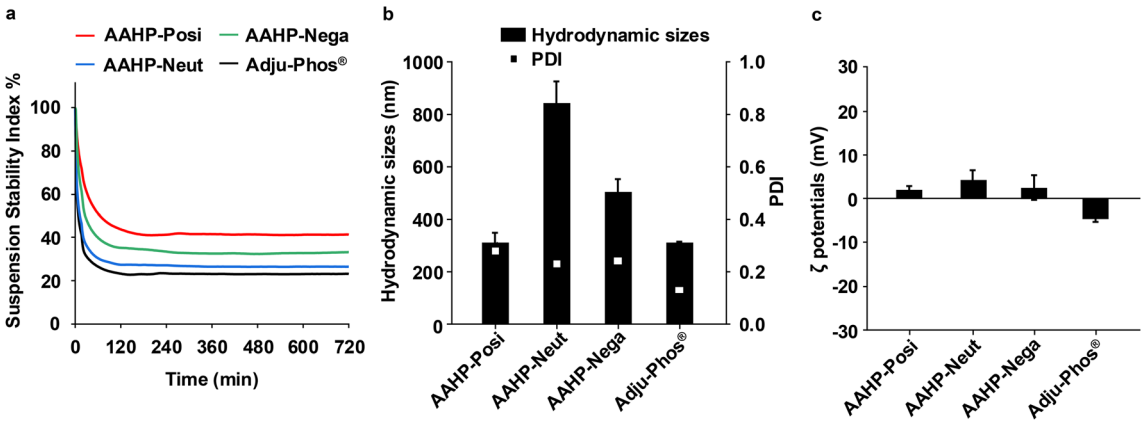

Fig. 4 Suspension stability of AAHP NP-antigen complexes. (a) Suspension stability index, (b) hydrodynamic sizes, PDI, and (c) ζ potentials of AAHP-antigen complexes. 49.5 μg mL^{-1} of HPV VLP 18 was mixed with 1.1 mg mL^{-1} of AAHP NPs, and the complexes were formulated in saline in the presence of 0.75 mg mL^{-1} of Tween 80.

To further investigate the suspension stability of aluminum-based adjuvants under formulation conditions, HPV VLP type 18 antigen was adsorbed on AAHP NPs in a saline buffer containing 0.75 mg mL^{-1} of Tween 80, and the suspension stability was monitored. It was shown that the suspension stability index exhibited a significant decline for all adjuvant-antigen complexes (Fig. 4a and Fig. S2†). This reduction in stability is likely attributed to the substantial increase in particle sizes and the near-neutral surface charges observed post-antigen adsorption (Fig. 4b and c). Although the adjuvant–antigen complexes sedimented rapidly, the synthesized AAHP-NPs demonstrated improved suspension stability compared to the commercially available Adju-Phos®. The enhanced vaccine efficacy of AAHP-Posi-formulated HPV VLP type 18 vaccines, as demonstrated in our prior study,[6] was critically dependent on their superior colloidal stability compared to AAHP-Neut, AAHP-Nega, and the commercial adjuvant Adju-Phos®. Notably, AAHP-Posi-adjuvanted VLPs induced significantly higher levels of HBV VLP-specific total IgG and IgG_1 antibodies than Adju-Phos®-adjuvanted formulations following a two-dose intramuscular immunization. This heightened immunogenicity is mechanistically linked to the capacity of AAHP-Posi to interact with cell membranes, triggering membrane perturbation accompanied by potassium efflux and enhanced antigen internalization. Subsequent downstream inflammatory responses were characterized by mitochondrial reactive oxygen species (ROS) generation and pro-inflammatory cytokine production, mediated through lysosomal damage *via* nanoparticle–phospholipid interactions. The immunostimulatory effects of AAHPs, governed by their surface charges, were further validated in murine vaccination models using *Staphylococcus aureus* (*S. aureus*) recombinant antigens, including MntC (manganese ion transport protein C) and mSEB (mutant staphylococcal enterotoxin B). AAHP-Posi elicited the most robust and durable antigen-specific antibody responses among all formulations. In a lethal challenge model with methicillin-resistant *S. aureus* (MRSA252), mice immunized with AAHP-Posi-adjuvanted mSEB exhibited a survival rate of 75%, significantly surpassing those adjuvanted with AAHP-Neut (62.5%), AAHP-Nega (37.5%), or Adju-Phos® (37.5%). These findings underscore the pivotal role of surface charge in dictating adjuvant activity, with positively charged AAHPs demonstrating superior efficacy in potentiating humoral immunity.

3.3 Suspension stability of AlOOH nanorods

Using a hydrothermal method, AlOOH nanorods with controlled aspect ratio were prepared.[7] The synthesized aluminum oxyhydroxide adjuvant showed the rod-like structures by TEM analysis (Fig. 5a), and their aspect ratios were determined as 41 and 7 by Image J, named Rod-H and Rod-L, respectively (Table 2). The AlOOH nanorods were then analyzed by XRD, which showed that they possessed a typical boehmite structure (Fig. 5b), similar to the commercially available adjuvant, Alhydrogel®.[7,37,38] The Rod-H and Rod-L exhibited a hydrodynamic size as 234 ± 7 and 89 ± 3 nm, respectively (Table 2). Both Rod-H and Rod-L are positively-charged particles, with ζ potentials of 43 ± 1 and 39 ± 3 mV respectively (Table 2). As a control, Alhydrogel® exhibited a rod-like morphology based on TEM, with a hydrodynamic size of 173 ± 13 nm and ζ potential of 24 ± 3 mV (Table 2).

The suspension stability of AlOOH nanorods was systematically investigated. As illustrated in Fig. 6a, the suspension stability index of Rod-H and Rod-L in water remained >80% after 12 hours, whereas Alhydrogel® exhibited a decline to 67%. This indicated that the in-house synthesized Rod-H and Rod-L possess superior suspension stability compared to the commercial adjuvant, Alhydrogel®. This enhanced stability can be attributed to the higher ζ potentials of Rod-H and Rod-L in water, which provide stronger electrostatic repulsion, thereby maintaining the stability. Moreover, sedimentation and aggregation processes are driven by the tendency of the system to minimize its energy. It has been reported that particles with higher SFE are more prone to aggregation as a

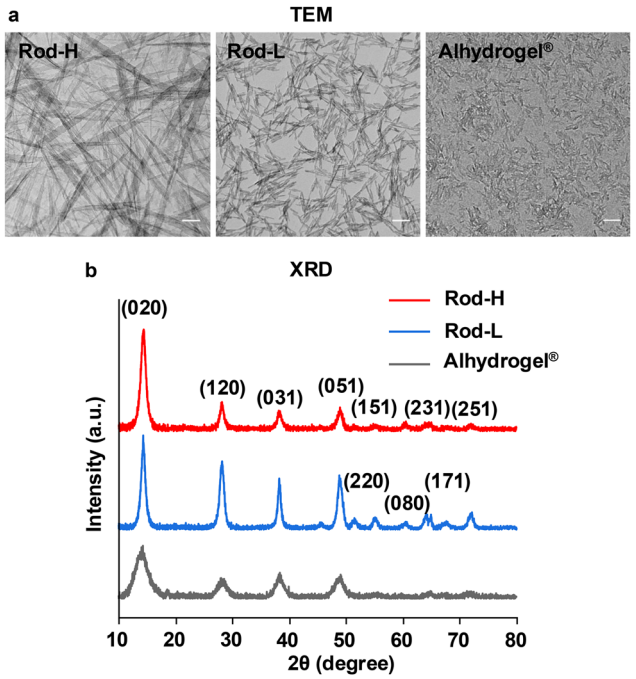

Fig. 5 Characterization of AlOOH nanorods. (a) TEM analysis of AlOOH nanorods. Scale bar is 100 nm. (b) XRD analysis of AlOOH nanorods. Alhydrogel® is used as a control.

means of reducing the overall system energy.[19,36,39] To further elucidate the factors that affect the suspension stability of AlOOH nanorods, the SFE was measured using the maximum particle dispersion method.[20,40,41] The SFE values for Rod-H and Rod-L were determined to be 33 and 51 mJ m^{-2}, respectively (Fig. 6b and Fig. S3, ESI†). In contrast, Alhydrogel® has been reported to exhibit a higher SFE of 55 mJ m^{-2},[19] which may account for its rapid sedimentation rate in aqueous suspension.

The suspension stabilities of AlOOH nanorods in saline buffer were further investigated (Fig. 6c). Rod-H and Rod-L exhibited exceptional stabilities over a 12-hour period, while the suspension stability index of Alhydrogel® declined to 1% within 2 hours. Under saline conditions, all particles exhibited an increase in hydrodynamic size (Fig. 6d), and their ζ potentials decreased to approximately 10–20 mV (Fig. 6e). For Alhydrogel®, its high SFE predisposed it to aggregation, and the observed changes in particle size and ζ potential in saline further accelerated its aggregation and sedimentation. Interestingly, although both Rod-H and Rod-L experienced a reduction in ζ potential in saline buffer, the decrease was less pronounced for Rod-L compared to Rod-H. Based on previous studies,[42–44] the density of surface hydroxyl (-OH) groups on γ-AlOOH follows the order (010) > (001) > (100), and anions such as Cl^- preferentially adsorb onto the (010) and (001) facets through the interactions with surface –OH groups. Consequently, it could be deduced that in saline, Cl^- adsorbed on the (010) and (001) facets of Rod-H, leading to a significant reduction in ζ potential from 43 in water to 11 mV in saline. In contrast, Rod-L exhibited less exposed (010) and (001) facets, as evidenced by the ratio of the (020)/(120) peak area in XRD analysis (Fig. 5b), with ratios of 4.63 and 1.28 for Rod-H and Rod-L, respectively. This lower facet exposure resulted in reduced Cl^- adsorption on Rod-L, explaining the comparatively smaller decrease in its ζ potential.

In addition, it was observed that the stability of Rod-H in saline was even better than in water. For AlOOH nanorods, the (010) face exhibits the lowest surface energy. Consequently, the (010) facets of Rod-H in saline were not fully exposed after Cl^-adsorption, potentially leading to an increase in SFE compared to that in water. This change may reduce the hydrophobicity of Rod-H, as the interfacial energy between the particles and water decreases when the SFE rises, resulting in a more hydrophilic surface in saline.[7,45] To validate this, the surface hydrophobicity of Rod-H was assessed using pyrene method, showing the lower level of hydrophobicity in saline compared to that in H_2O (Fig. S4, ESI†), which effectively mitigated the particle aggregation and sedimentation of Rod-H in saline environments.[46–48] Collectively, these observations indicate that the suspension stability of AlOOH nanorods is governed by a complex interplay of multiple factors, including particle sizes, ζ potential, SFE, and surface hydrophobicity.

Furthermore, the suspension stability of AlOOH-antigen complexes was systematically evaluated. As illustrated in Fig. 6f, the suspension stability index for all three AlOOH-BSA complexes declined to 12% or below within 2 hours. This was accompanied by a significant increase in the hydrodynamic diameters of the adjuvant-antigen complexes (Fig. 6g), a trend consistent with observations in AAHP NPs-antigen complexes. This accelerated sedimentation behavior aligns with the principles of Stokes' law.[18] Additionally, the ζ potentials of the complexes were found to approach 0 mV (Fig. 6h), a condition that is thermodynamically unfavorable for particle stability. Notably, Rod-H-BSA and Rod-L-BSA exhibited superior suspension stability compared to Alhydrogel®-BSA, suggesting that the intrinsic properties of AlOOH nanorods play a critical role in determining the stability of the AlOOH-BSA complexes.

To systematically evaluate the impact of intrinsic physicochemical properties of AlOOH nanorods on the suspension

Table 2 Hydrodynamic size and ζ potential of AlOOH nanorods suspended in water measured by dynamic light scattering (DLS)

Sample ID	Aspect ratio	Hydrodynamic sizes in water (nm)	Polydispersity index	Zeta potential in water (mV)
Rod-H	41	234 ± 7	0.26 ± 0.01	+43 ± 1
Rod-L	7	89 ± 3	0.17 ± 0.02	+39 ± 3
Alhydrogel®	7	173 ± 13	0.29 ± 0.01	+24 ± 3

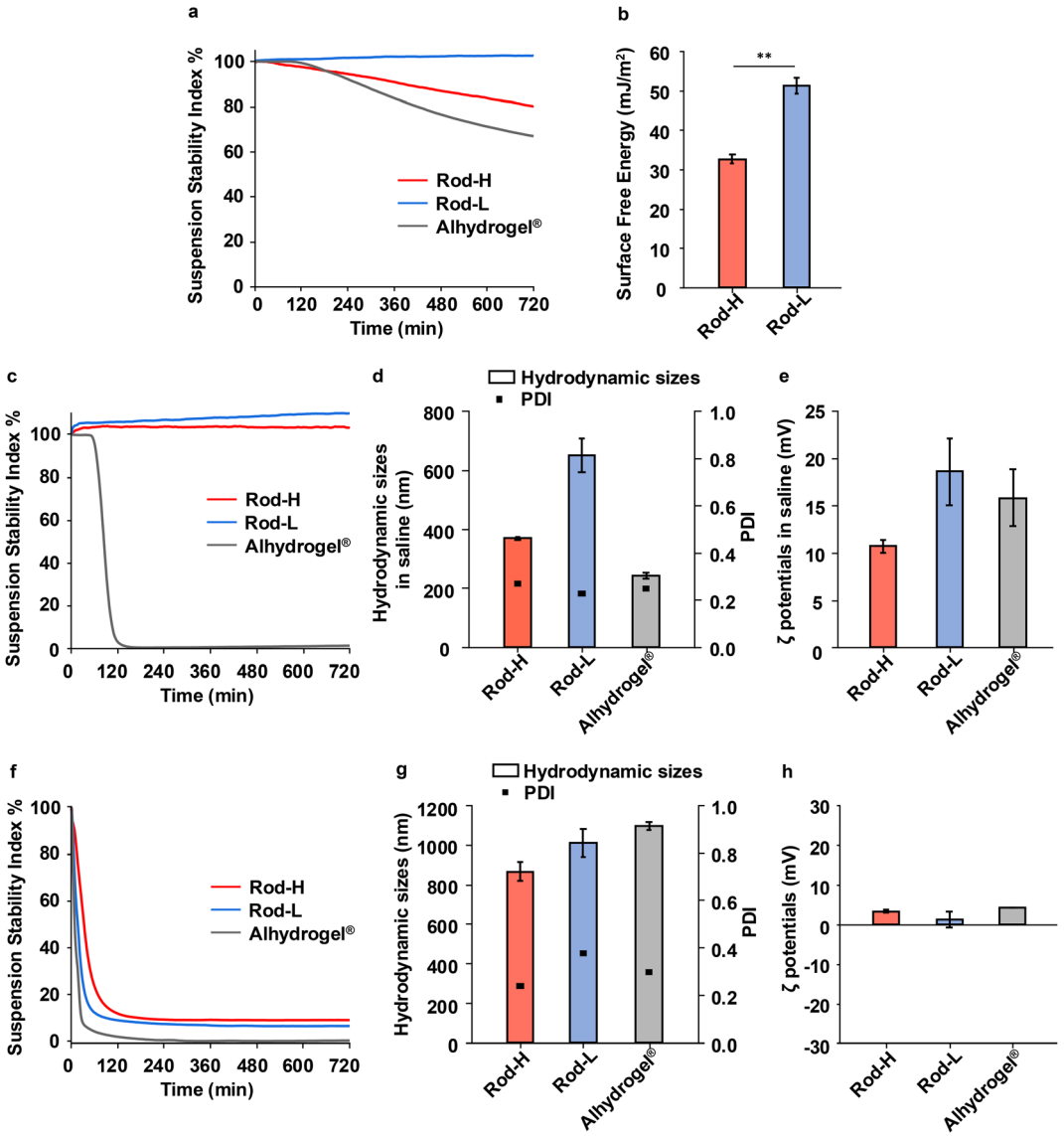

Fig. 6 Suspension stability of AlOOH nanorods and AlOOH-antigen complexes. (a) Suspension stability index of AlOOH nanorods in water. (b) Surface free energy of Rod-H and Rod-L. (c) Suspension stability index, (d) hydrodynamic sizes, PDI, and (e) ζ potentials of AlOOH nanorods in saline. (f) Suspension stability index, (g) hydrodynamic sizes, PDI, and (h) ζ potentials of AlOOH-antigen complexes. 49.5 μg mL^{-1} of BSA was formulated with 1.1 mg mL^{-1} of AlOOH nanorods in saline buffer containing 0.75 mg mL^{-1} of Tween 80. *p < 0.05, **p < 0.01, ***p < 0.001.

stability of AlOOH-antigen complexes and their resultant vaccine efficacy, we evaluate two model antigens, SARS-CoV-2 receptor-binding domain (RBD) and Hepatitis B surface antigen virus-like particles (HBsAg VLPs), in a comparative *in vivo* immunization study.[7] Our findings demonstrated that high-aspect-ratio AlOOH nanorods exhibit superior immunogenicity, eliciting significant higher antigen-specific antibody titers in murine serum comparted to the low-aspect ratio nanorods following a two-dose intramuscular immunization. These enhancement in humoral immune responses were positively correlated with improved suspension stability of the antigen-nanorod complexes. Furthermore, adjuvant efficacy is influenced by multiple physicochemical parameters beyond suspension stability. As demonstrated in previous studies, high-aspect-ratio AlOOH nanorods (Rod-H) possess lower surface free energy (SFE), conferring enhanced surface hydrophobicity that facilitates stronger interactions with cellular membranes. This was quantitatively verified through quartz crystal microbalance with dissipation monitoring (QCM-D) analyses of nanorod binding kinetics with biomimetic phospholipid bilayers. The combined effects of these material properties enable Rod-H to more effectively promote membrane depolarization more effectively, enhance cellular uptake, and activate dendritic cells (DCs), ultimately driving superior humoral immunity in both SARS-CoV-2 and HBV vaccine models. These findings establish a structure–activity relationship where nanorod morphology directly modulates antigen delivery efficiency and immunopotentiation capacity, providing critical

guidance for the rational design of AlOOH-based vaccine adjuvants.

4. Conclusion

In this study, we systematically elucidated the key factors governing the suspension stability of aluminum-based adjuvants. For AAHP NPs, smaller particle size and higher surface charge were identified as critical parameters for maintaining their suspension stability. In the case of AlOOH nanorods, in addition to smaller particle size and higher surface charge, lower surface free energy and reduced hydrophobicity were found to significantly enhance their suspension stability. Furthermore, for formulated vaccines, improving the suspension stability of aluminum-based adjuvants demonstrated to a positive correlation with the stability of adjuvant-antigen complexes. These findings from our study provide a robust theoretical foundation for the rational design and selection of aluminum-based adjuvants in vaccine formulations, offering insights into optimizing their performance for enhanced vaccine efficacy.

Data availability

All data generated in this study are provided in the manuscript and its ESI.† Relevant data are available from the corresponding authors (Changying Xue and Bingbing Sun) upon reasonable request.

Conflicts of interest

The authors declare no conflict of interest.

Acknowledgements

This work was supported by the National Key Research and Development Program of China (2022YFC2304305), National Natural Science Foundation of China (U22A20455), and Fundamental Research Funds for the Central Universities (DUT22QU225 and DUT22LAB601).

References

1 P. He, Y. Zou and Z. Hu, *Hum. Vaccines Immunother.*, 2015, **11**, 477–488.
2 B. Pulendran, P. S. Arunachalam and D. T. O'Hagan, *Nat. Rev. Drug Discovery*, 2021, **20**, 454–475.
3 A. T. Glenny, C. G. Pope, H. Waddington and U. Wallace, *J. Pathol. Bacteriol.*, 1926, **29**, 31–40.
4 L. S. Burrell, C. T. Johnston, D. Schulze, J. Klein, J. L. White and S. L. Hem, *Vaccine*, 2000, **19**, 275–281.
5 L. S. Burrell, C. T. Johnston, D. Schulze, J. Klein, J. L. White and S. L. Hem, *Vaccine*, 2000, **19**, 282–287.
6 Z. Liang, Y. Yang, G. Yu, H. Zhu, X. Xia, C. Chen, D. Fu, M. Li, G. Cheng, C. Xue, L. Shi, H. Zeng and B. Sun, *Biomaterials*, 2021, **275**, 120960.
7 Z. Liang, X. Wang, G. Yu, M. Li, S. Shi, H. Bao, C. Chen, D. Fu, W. Ma, C. Xue and B. Sun, *Nano Today*, 2022, **43**, 101445.
8 L. A. Brito, P. Malyala and D. T. O'Hagan, *Semin. Immunol.*, 2013, **25**, 130–145.
9 T. Zhang, P. He, D. Guo, K. Chen, Z. Hu and Y. Zou, *Pharmaceutics*, 2023, **15**, 1756.
10 A. Langford, T. Horwitz, E. Adu-Gyamfi, C. Wiley, E. Holding, D. Zimmermann, A. A. Ignatius and S. Ohtake, *J. Pharm. Sci.*, 2020, **109**, 1460–1466.
11 K. Muthurania, A. A. Ignatius, Z. Jin, J. Williams and S. Ohtake, *J. Pharm. Sci.*, 2015, **104**, 3770–3781.
12 J.-F. Art, A. vander Straeten and C. C. Dupont-Gillain, *Int. J. Pharm.*, 2017, **517**, 226–233.
13 Y. Lu and G. Liu, *Hum. Vaccines Immunother.*, 2022, **18**, 2060667.
14 J. Guo, L. M. Lewis, H. Billones, E. Torres and P. Kolhe, *J. Pharm. Sci.*, 2016, **105**, 2009–2013.
15 L. M. Lewis, J. Guo, E. Torres, J. Wang, H. Billones, P. Kolhe, A. L. Young, D. Bates, A. Parker and S. Rigby-Singleton, *J. Pharm. Sci.*, 2017, **106**, 2163–2167.
16 O. O. Kolade, W. Jin, C. Tengroth, K. D. Green and D. G. Bracewell, *J. Pharm. Sci.*, 2015, **104**, 378–387.
17 P. Krishnamoorthy, *Int. J. Sediment Res.*, 2010, **25**, 119–133.
18 J. Duffy, M. Larsson and A. Hill, *Annu. Trans. Nord. Rheol. Soc.*, 2012, **20**, 209–214.
19 S. Bi, M. Li, Z. Liang, G. Li, G. Yu, J. Zhang, C. Chen, C. Yang, C. Xue, Y. Y. Zuo and B. Sun, *J. Colloid Interface Sci.*, 2022, **627**, 238–246.
20 Z. Cao, S. N. Tsai and Y. Y. Zuo, *Anal. Chem.*, 2019, **91**, 12819–12826.
21 T. Li, Q. Zhong, B. Zhao, S. Lenaghan, S. Wang and T. Wu, *Carbohydr. Polym.*, 2020, **234**, 115863.
22 M. M. Amiji, *Carbohydr. Polym.*, 1995, **26**, 211–213.
23 B. Wang, W. Zhang, X. Bai, C. Li and D. Xiang, *Food Hydrocolloids*, 2020, **103**, 105706.
24 Y. Ma, Y. Guo, S. Liu, Y. Hu, C. Yang, G. Cheng, C. Xue, Y. Y. Zuo and B. Sun, *Nano Lett.*, 2023, **23**, 7552–7560.
25 I. Ostolska and M. Wiśniewska, *Colloid Polym. Sci.*, 2014, **292**, 2453–2464.
26 B. Özbek and Ş. Ünal, *Korean J. Chem. Eng.*, 2017, **34**, 1992–2001.
27 R. Pamies, J. G. H. Cifre, V. F. Espín, M. Collado-González, F. G. D. Baños and J. G. de la Torre, *J. Nanopart. Res.*, 2014, **16**, 2376.
28 T. Kim, C.-H. Lee, S.-W. Joo and K. Lee, *J. Colloid Interface Sci.*, 2008, **318**, 238–243.
29 S. Dong, Z. Zeng, W. Cai, Z. Zhou, C. Dou, H. Liu and J. Xia, *J. Nanopart. Res.*, 2019, **21**, 233.
30 G. I. Guerrero-García, E. González-Tovar and M. O. De La Cruz, *Soft Matter*, 2010, **6**, 2056–2065.

31 M. Zareei, H. Yoozbashizadeh and H. R. Madaah Hosseini, *J. Therm. Anal. Calorim.*, 2019, **135**, 1185–1196.
32 E. J. W. Verwey, *J. Phys. Colloid Chem.*, 1947, **51**, 631–636.
33 B. Derjaguin and L. Landau, *Prog. Surf. Sci.*, 1993, **43**, 30–59.
34 D. Zhou, Z. Ji, X. Jiang, D. R. Dunphy, J. Brinker and A. A. Keller, *PLoS One*, 2013, **8**, e81239.
35 I. Ojea-Jiménez and V. Puntes, *J. Am. Chem. Soc.*, 2009, **131**, 13320–13327.
36 S. U. Ilyas, R. Pendyala and N. Marneni, *Chem. Eng. Technol.*, 2014, **37**, 2011–2021.
37 X. Y. Chen, Z. J. Zhang, X. L. Li and S. W. Lee, *Solid State Commun.*, 2008, **145**, 368–373.
38 K. Mahmoodi and B. Alinejad, *Powder Technol.*, 2010, **199**, 289–292.
39 S. Witharana, I. Palabiyik, Z. Musina and Y. Ding, *Powder Technol.*, 2013, **239**, 72–77.
40 G. Li, Z. Cao, K. K. H. Y. Ho and Y. Y. Zuo, *Anal. Chem.*, 2022, **94**, 2078–2086.
41 G. Li, K. K. H. Y. Ho and Y. Y. Zuo, *J. Phys. Chem. C*, 2022, **126**, 832–837.
42 T. He, L. Xiang and S. Zhu, *CrystEngComm*, 2009, **11**, 1338–1342.
43 W. Jiao, X. Wu, T. Xue, G. Li, W. Wang, Y. Wang, Y. Wang, Y. Tang and M.-Y. He, *Cryst. Growth Des.*, 2016, **16**, 5166–5173.
44 Y. Xia, X. Jiao, Y. Liu, D. Chen, L. Zhang and Z. Qin, *J. Phys. Chem. C*, 2013, **117**, 15279–15286.
45 Y. Tian and L. Jiang, *Nat. Mater.*, 2013, **12**, 291–292.
46 B. Yang and S. Song, *Surf. Rev. Lett.*, 2014, **21**, 1430003.
47 S. Lu and S. Song, *Colloids Surf.*, 1991, **57**, 49–60.
48 P. Yang, X. Hu, F. Zi, B. Yang, Q. Wang, Y. Chen and S. Chen, *Miner. Eng.*, 2020, **155**, 106444.